

Optical Engineering

OpticalEngineering.SPIEDigitalLibrary.org

Review of nonlinear ultrasonic guided wave nondestructive evaluation: theory, numerics, and experiments

Vamshi Krishna Chillara
Cliff J. Lissenden

Review of nonlinear ultrasonic guided wave nondestructive evaluation: theory, numerics, and experiments

Vamshi Krishna Chillara and Cliff J. Lissenden*

The Pennsylvania State University, Department of Engineering Science and Mechanics, University Park, Pennsylvania 16802, United States

Abstract. Interest in using the higher harmonic generation of ultrasonic guided wave modes for nondestructive evaluation continues to grow tremendously as the understanding of nonlinear guided wave propagation has enabled further analysis. The combination of the attractive properties of guided waves with the attractive properties of higher harmonic generation provides a very unique potential for characterization of incipient damage, particularly in plate and shell structures. Guided waves can propagate relatively long distances, provide access to hidden structural components, have various displacement polarizations, and provide many opportunities for mode conversions due to their multimode character. Moreover, higher harmonic generation is sensitive to changing aspects of the microstructures such as to the dislocation density, precipitates, inclusions, and voids. We review the recent advances in the theory of nonlinear guided waves, as well as the numerical simulations and experiments that demonstrate their utility. © 2015 Society of Photo-Optical Instrumentation Engineers (SPIE) [DOI: [10.1117/1.OE.55.1.011002](https://doi.org/10.1117/1.OE.55.1.011002)]

Keywords: nonlinear ultrasonics; guided waves; higher harmonic generation.

Paper 150688SSV received May 25, 2015; accepted for publication Jul. 10, 2015; published online Aug. 19, 2015.

1 Introduction

Nonlinear ultrasonic nondestructive evaluation uses interrogation signals at frequencies other than the excitation frequency to detect changes in structural integrity and characterize degradation of materials. Nonlinear ultrasonic methodologies provide improved sensitivity to damage and the ability to identify incipient damage relative to linear methods. In general, linear ultrasonic methods provide good sensitivity to macroscale damage such as long fatigue cracks. However, in many cases, once damage appears at the macroscale, the remaining life is short, severely limiting maintenance decisions. Thus, characterization of incipient damage could facilitate a paradigm shift in operations of structural systems from schedule-based to condition-based maintenance that would ultimately enhance safety and reduce life cycle costs. Nonlinear ultrasonics is a broad discipline^{1,2} which encompasses many specialized techniques reliant upon nonlinear material behavior to detect and/or characterize incipient damage. Some of these include nonlinear resonant ultrasound spectroscopy,³ nonlinear elastic wave spectroscopy,⁴⁻⁶ and second-harmonic generation.⁷ Modeling relies upon both classical and nonclassical⁸ nonlinear effects such as hysteresis. Early investigations focused on using higher harmonic generation for characterizing material microstructure.⁹⁻¹¹ The contributions of elastic nonlinearity and dislocations were examined for bulk waves.¹²⁻¹⁴ Many studies over the years have employed second-harmonic generation to characterize microstructural changes, for example, associated with fatigue, creep, or thermal aging. A recent article¹⁵ provides a thorough review of second-harmonic generation measurements. The overwhelming majority of the work reviewed in Refs. 1, 2, and 15 involves

bulk waves, and to a lesser extent, Rayleigh surface waves. However, over the course of the last 15 to 20 years, nonlinear ultrasonic guided waves have emerged as a powerful tool for characterization of incipient damage in structures comprised plates, pipes/tubes, rods, and rails. The advantages of nonlinear guided waves are the union of the advantages of nonlinear ultrasonics already described (i.e., improved sensitivity and capability to detect incipient damage) and guided waves (e.g., volumetric coverage, long propagation distances, single-sided access, inspection speed, and inspection of inaccessible domains). Further advantages could be realized by implementing noncontact methods such as laser excitation and laser Doppler vibrometer measurements. However, due to the dispersive multimodal character of guided waves, they present a number of analytical challenges that bulk waves do not, and the likelihood of performing a successful inspection with nonlinear guided waves without understanding their propagation is just above nil.

In this article, theoretical modeling of nonlinear guided wave propagation is summarized first in Sec. 2. Doing so enables intelligent selection of primary wave modes that will generate strong internally resonant higher harmonics through interaction with the nonlinear elastic waveguide. Numerical simulations provide a means to test assumptions made in the model development and enable demonstration of nonlinear wave propagation features without the additional nonlinearities introduced by laboratory instrumentation. Thus, results of finite element analyses are reviewed in Sec. 3. Experiments provide the only real proof of the veracity of the theory and simulations. Thus, Sec. 4 reviews results from higher harmonic generation experiments on waveguide structures. These experimental results demonstrate

*Address all correspondence to: Cliff J. Lissenden, E-mail: lissenden@psu.edu

the unique wave propagation characteristic of internally resonant higher harmonics; their cumulative nature. They also show how the higher harmonics generation changes as the material microstructure changes. The article closes with a summary and discussion of where the current state-of-knowledge could lead.

2 Theory

In Sec. 1, we provided the motivation for using nonlinear guided waves for microscale damage detection and characterization. However, the mathematical complexity associated with guided wave propagation does not easily lend itself for analysis from a theoretical standpoint. A first step in this regard was taken by Deng^{16,17} to analyze the second-harmonic guided wave generation from shear-horizontal (SH) and Rayleigh–Lamb (RL) modes in plates. The approach was based on the use of the partial-wave technique¹⁸ to expand the primary wave-field, and then to examine the conditions under which the second harmonics from partial waves generate a propagating guided wave field. De Lima and Hamilton¹⁹ employed a different approach to analyze second-harmonic generation from guided waves in plates. In this section, we describe their approach to study second-harmonic guided wave generation in plates. Unlike the study by De Lima and Hamilton,¹⁹ we adopt a displacement gradient-based formulation that enables a systematic analysis procedure. Next, we introduce some notation that is used in the rest of the article.

2.1 Notation

We used bold letters to denote vectors and tensors and denote the position of the material particle in the reference and current configurations²⁰ by \mathbf{X} and \mathbf{x} , respectively. The displacement of the material particles is denoted by \mathbf{u} . The deformation gradient is denoted by \mathbf{F} and is given by

$$\mathbf{F} = \frac{\partial \mathbf{x}}{\partial \mathbf{X}}. \quad (1)$$

Likewise, the displacement gradient is denoted by \mathbf{H} and is given by

$$\mathbf{H} = \frac{\partial \mathbf{u}}{\partial \mathbf{X}} = \mathbf{F} - \mathbf{I}, \quad (2)$$

where \mathbf{I} is the identity tensor. We use a Lagrangian measure of strain denoted by \mathbf{E} and given by

$$\mathbf{E} = \frac{1}{2}(\mathbf{F}^T \mathbf{F} - \mathbf{I}) = \frac{1}{2}(\mathbf{H} + \mathbf{H}^T + \mathbf{H}^T \mathbf{H}). \quad (3)$$

Also, the linearized strain that does not include geometric nonlinearity is denoted by \mathbf{E}_{lin} and is given by

$$\mathbf{E}_{\text{lin}} = \frac{1}{2}(\mathbf{H} + \mathbf{H}^T). \quad (4)$$

In this article, two equivalent (widely used) weakly nonlinear hyperelastic constitutive models that describe the strain energy function of the material are used and are given by

1. Landau–Lifshitz model

$$W(\mathbf{E}) = \frac{1}{2} \lambda [\text{tr}(\mathbf{E})]^2 + \mu \text{tr}(\mathbf{E}^2) + \frac{1}{3} C [\text{tr}(\mathbf{E})]^3 + B \text{tr}(\mathbf{E}) \text{tr}(\mathbf{E}^2) + \frac{1}{3} A \text{tr}(\mathbf{E}^3). \quad (5)$$

2. Murnaghan model

$$W(\mathbf{E}) = \frac{1}{2} \lambda [\text{tr}(\mathbf{E})]^2 + \mu \text{tr}(\mathbf{E}^2) + \frac{1}{3} (l + 2m) [\text{tr}(\mathbf{E})]^3 - m \text{tr}(\mathbf{E}) \{ [\text{tr}(\mathbf{E})]^2 - \text{tr}(\mathbf{E}^2) \} + n \det(\mathbf{E}). \quad (6)$$

Here, λ, μ are the Lamé's constants, A, B, C are called the third order elastic constants, and l, m, n are called the Murnaghan constants. The constants (A, B, C) and (l, m, n) are related by²¹ $l = B + C$, $m = (1/2)A + B$, and $n = A$. Next, we introduce some stress measures used in this article. First, the second Piola–Kirchhoff stress tensor (\mathbf{T}_{RR}) is obtained from $\mathbf{W}(\mathbf{E})$ and is given by

$$\mathbf{T}_{\text{RR}} = \frac{\partial \mathbf{W}(\mathbf{E})}{\partial \mathbf{E}}. \quad (7)$$

The first Piola–Kirchhoff stress (\mathbf{S}) is related to \mathbf{T}_{RR} by

$$\mathbf{S} = \mathbf{F} \mathbf{T}_{\text{RR}}. \quad (8)$$

For the Landau–Lifshitz model, the second Piola–Kirchhoff stress tensor is written in terms of strain as

$$\mathbf{T}_{\text{RR}}(\mathbf{E}) = \lambda \text{tr}(\mathbf{E}) + 2\mu \mathbf{E} + C [\text{tr}(\mathbf{E})]^2 \mathbf{I} + B \text{tr}(\mathbf{E}^2) \mathbf{I} + 2B \text{tr}(\mathbf{E}) \mathbf{E} + A \mathbf{E}^2. \quad (9)$$

Since our theoretical formulation is based on the displacement gradient, we treat first and second Piola–Kirchhoff stress tensors as explicit functions of displacement gradient (\mathbf{H}) and they are denoted as $\mathbf{S}(\mathbf{H})$ and $\mathbf{T}_{\text{RR}}(\mathbf{H})$. $\mathbf{T}_{\text{RR}}(\mathbf{H})$ can be obtained by using Eqs. (9) and (3) and is given by

$$\begin{aligned} \mathbf{T}_{\text{RR}}(\mathbf{H}) = & \frac{\lambda}{2} \text{tr}(\mathbf{H} + \mathbf{H}^T) + \mu (\mathbf{H} + \mathbf{H}^T) + \frac{\lambda}{2} \text{tr}(\mathbf{H}^T \mathbf{H}) \mathbf{I} \\ & + C \text{tr}(\mathbf{H})^2 \mathbf{I} + \mu \mathbf{H}^T \mathbf{H} + B \text{tr}(\mathbf{H})(\mathbf{H} + \mathbf{H}^T) \\ & + \frac{B}{2} \text{tr}(\mathbf{H}^2 + \mathbf{H}^T \mathbf{H}) \mathbf{I} + \frac{A}{4} (\mathbf{H}^2 + \mathbf{H}^T \mathbf{H} + \mathbf{H} \mathbf{H}^T + \mathbf{H}^T \mathbf{H}^2), \end{aligned} \quad (10)$$

up to second order in \mathbf{H} . Further, we decompose $\mathbf{T}_{\text{RR}}(\mathbf{H})$ into two parts, namely $\mathbf{T}_{\text{RR}}^{\text{L}}(\mathbf{H})$ and $\mathbf{T}_{\text{RR}}^{\text{NL}}(\mathbf{H})$ such that $\mathbf{T}_{\text{RR}}(\mathbf{H}) = \mathbf{T}_{\text{RR}}^{\text{L}}(\mathbf{H}) + \mathbf{T}_{\text{RR}}^{\text{NL}}(\mathbf{H})$. As indicated in the notation, $\mathbf{T}_{\text{RR}}^{\text{L}}(\mathbf{H})$ is linear in \mathbf{H} and $\mathbf{T}_{\text{RR}}^{\text{NL}}(\mathbf{H})$ is nonlinear in \mathbf{H} and is explicitly given by

$$\begin{aligned}\mathbf{T}_{\mathbf{RR}}^{\mathbf{L}}(\mathbf{H}) &= \frac{\lambda}{2} \text{tr}(\mathbf{H} + \mathbf{H}^{\mathbf{T}}) \mathbf{I} + \mu(\mathbf{H} + \mathbf{H}^{\mathbf{T}}), \\ \mathbf{T}_{\mathbf{RR}}^{\mathbf{NL}}(\mathbf{H}) &= \frac{\lambda}{2} \text{tr}(\mathbf{H}^{\mathbf{T}} \mathbf{H}) \mathbf{I} + C \text{tr}(\mathbf{H})^2 \mathbf{I} + \mu \mathbf{H}^{\mathbf{T}} \mathbf{H} + B \text{tr}(\mathbf{H})(\mathbf{H} + \mathbf{H}^{\mathbf{T}}) \\ &+ \frac{B}{2} \text{tr}(\mathbf{H}^2 + \mathbf{H}^{\mathbf{T}} \mathbf{H}) \mathbf{I} + \frac{A}{4} (\mathbf{H}^2 + \mathbf{H}^{\mathbf{T}} \mathbf{H} + \mathbf{H} \mathbf{H}^{\mathbf{T}} + \mathbf{H}^{\mathbf{T}2}).\end{aligned}\quad (11)$$

Likewise, using $\mathbf{S} = \mathbf{F} \mathbf{T}_{\mathbf{RR}}$, we can write $\mathbf{S}(\mathbf{H}) = \mathbf{S}^{\mathbf{L}}(\mathbf{H}) + \mathbf{S}^{\mathbf{NL}}(\mathbf{H})$ where

$$\mathbf{S}^{\mathbf{L}}(\mathbf{H}) = \mathbf{T}_{\mathbf{RR}}^{\mathbf{L}}(\mathbf{H}),$$

and

$$\mathbf{S}^{\mathbf{NL}}(\mathbf{H}) = \mathbf{H} \mathbf{T}_{\mathbf{RR}}^{\mathbf{L}}(\mathbf{H}) + \mathbf{T}_{\mathbf{RR}}^{\mathbf{NL}}(\mathbf{H}). \quad (12)$$

Equivalent expressions can be obtained for the Murnaghan model. However, we restrict ourselves to the Landau–Lifshitz model in this section.

2.2 Second-Harmonic Guided Waves in Plates

Consider the schematic of the traction-free plate in the reference configuration as shown in Fig. 1. We begin with the referential form of the balance of the linear momentum given by

$$\text{Div}[\mathbf{S}(\mathbf{H})] = \rho_{\kappa} \ddot{\mathbf{u}}, \quad \mathbf{S} \mathbf{n}_{\kappa} = \mathbf{0} \quad \text{on} \quad \mathbf{X}_2 = \pm \mathbf{h}, \quad (13)$$

where \mathbf{n}_{κ} denotes the unit normal to the surface of the plate in the reference configuration and ρ_{κ} denotes the density of the material in the reference configuration.

Suppose that the displacement associated with the primary wave propagating in the plate is denoted by $\mathbf{u}_1(\mathbf{X}, \mathbf{t})$, and that associated with the secondary wavefield is denoted by $\mathbf{u}_2(\mathbf{X}, \mathbf{t})$, then the total displacement in the material is given by

$$\mathbf{u}(\mathbf{X}, \mathbf{t}) = \mathbf{u}_1(\mathbf{X}, \mathbf{t}) + \mathbf{u}_2(\mathbf{X}, \mathbf{t}) \quad \text{with} \quad \|\mathbf{u}_2\| \ll \|\mathbf{u}_1\|, \quad (14)$$

where the perturbation assumption is indicated. Likewise for the displacement gradient, we have

$$\mathbf{H} = \mathbf{H}_1 + \mathbf{H}_2 \quad \text{with} \quad \|\mathbf{H}_2\| \ll \|\mathbf{H}_1\|, \quad (15)$$

where $\mathbf{H}_1 = (\partial \mathbf{u}_1 / \partial \mathbf{X})$ and $\mathbf{H}_2 = (\partial \mathbf{u}_2 / \partial \mathbf{X})$ are the displacement gradients associated with primary and secondary displacements. Next, we obtain the expression for the first-Piola Kirchhoff stress that goes into Eq. (13). Using Eq. (12), we get

$$\begin{aligned}\mathbf{S}(\mathbf{H}) &= \mathbf{S}^{\mathbf{L}}(\mathbf{H}) + \mathbf{S}^{\mathbf{NL}}(\mathbf{H}) \Rightarrow \\ \mathbf{S}(\mathbf{H}_1 + \mathbf{H}_2) &= \mathbf{S}^{\mathbf{L}}(\mathbf{H}_1 + \mathbf{H}_2) + \mathbf{S}^{\mathbf{NL}}(\mathbf{H}_1 + \mathbf{H}_2) \Rightarrow \\ \mathbf{S}(\mathbf{H}_1 + \mathbf{H}_2) &= \mathbf{S}^{\mathbf{L}}(\mathbf{H}_1) + \mathbf{S}^{\mathbf{L}}(\mathbf{H}_2) + \mathbf{S}^{\mathbf{NL}}(\mathbf{H}_1 + \mathbf{H}_2),\end{aligned}\quad (16)$$

where the linearity of $\mathbf{S}^{\mathbf{L}}(\mathbf{H})$ was used.

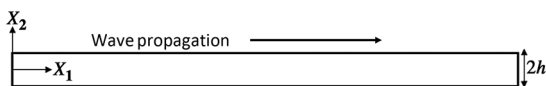


Fig. 1 Cross section of the traction-free plate.

As we are interested in the solution for the second harmonic, we retain only the terms of the second degree in \mathbf{H}_1 in the expression for $\mathbf{S}^{\mathbf{NL}}(\mathbf{H}_1 + \mathbf{H}_2)$, and denote those terms by $\mathbf{S}^{\mathbf{NL}}(\mathbf{H}_1, \mathbf{H}_1, 2)$ which correspond to self-interaction²² of the primary mode. From Eq. (16), we have

$$\mathbf{S}(\mathbf{H}) = \mathbf{S}^{\mathbf{L}}(\mathbf{H}_1) + \mathbf{S}^{\mathbf{L}}(\mathbf{H}_2) + \mathbf{S}^{\mathbf{NL}}(\mathbf{H}_1, \mathbf{H}_1, 2). \quad (17)$$

Substituting Eqs. (14) and (17) in Eq. (13), we obtain two separate boundary value problems for \mathbf{u}_1 and \mathbf{u}_2 as follows:

$$\text{Div}[\mathbf{S}^{\mathbf{L}}(\mathbf{H}_1)] - \rho_{\kappa} \ddot{\mathbf{u}}_1 = \mathbf{0} \quad \mathbf{S}^{\mathbf{L}}(\mathbf{H}_1) \mathbf{n}_{\kappa} = \mathbf{0}, \quad (18)$$

$$\begin{aligned}\text{Div}[\mathbf{S}^{\mathbf{L}}(\mathbf{H}_2)] - \rho_{\kappa} \ddot{\mathbf{u}}_2 &= -\text{Div}[\mathbf{S}^{\mathbf{NL}}(\mathbf{H}_1, \mathbf{H}_1, 2)] \\ \mathbf{S}^{\mathbf{L}}(\mathbf{H}_2) \mathbf{n}_{\kappa} &= -\mathbf{S}^{\mathbf{NL}}(\mathbf{H}_1, \mathbf{H}_1, 2) \mathbf{n}_{\kappa}.\end{aligned}\quad (19)$$

Now, assume $\mathbf{u}_1(\mathbf{X}, \mathbf{t}) = \text{Re}\{\mathbf{u}_1(\mathbf{X}_2) e^{i(\mathbf{k}\mathbf{X}_1 - \omega t)}\}$, a propagating guided wave mode in the plate (can either be RL or SH mode), where $\text{Re}\{\}$ denotes the real part of the argument, ω denotes the angular frequency, and k denotes the wavenumber of the mode. The first problem in Eq. (18) is identically satisfied due to our assumption that \mathbf{u}_1 is a propagating mode in the plate. On the other hand, the solution for \mathbf{u}_2 is obtained using the normal mode expansion technique.¹⁸ Following De Lima and Hamilton,¹⁹ we seek asymptotic expansions of $\mathbf{S}^{\mathbf{L}}(\mathbf{H}_2)$ and $\dot{\mathbf{u}}_2$ as follows:

$$\mathbf{S}^{\mathbf{L}}(\mathbf{H}_2) = \sum_{m=1}^{m=\infty} \mathbf{A}_m(\mathbf{X}_1) \mathbf{S}_m, \quad \dot{\mathbf{u}}_2 = \sum_{m=1}^{m=\infty} \mathbf{A}_m(\mathbf{X}_1) \mathbf{v}_m, \quad (20)$$

where $\mathbf{S}_{m=1}^{m=\infty}$ and $\mathbf{v}_{m=1}^{m=\infty}$ denote the stress and velocity fields corresponding to all the guided wave modes [propagating and nonpropagating (evanescent)] at 2ω .

As shown in Ref. 19, $A_m(X_1)$ satisfies the following ordinary differential equation [Eq. (21)] for each n such that $P_{mn} \neq 0$

$$4P_{mn} \left(\frac{\partial A_m}{\partial X_1} - ik_n^* X_1 \right) = (f_n^{\text{surf}} + f_n^{\text{vol}}). \quad (21)$$

Here,

$$\begin{aligned}P_{mn} &= \frac{-1}{4} \int_{-h}^h \left(\frac{\mathbf{S}_m \mathbf{v}_n^* + \mathbf{S}_n \mathbf{v}_m^*}{4} \cdot \mathbf{n}_1 \right) dX_2, \\ f_n^{\text{surf}} &= \frac{-1}{2} \mathbf{S}^{\mathbf{NL}}(\mathbf{H}_1, \mathbf{H}_1, 2) \mathbf{v}_n^* \cdot \mathbf{n}_2 \Big|_{-h}^h \\ f_n^{\text{vol}} &= \frac{1}{2} \int_{-h}^h \text{Div}[\mathbf{S}^{\mathbf{NL}}(\mathbf{H}_1, \mathbf{H}_1, 2)] \cdot \mathbf{v}_n^* dX_2.\end{aligned}\quad (22)$$

For every propagating mode m used in the asymptotic expansion, there is only one propagating mode $n = m$ such that $P_{mn} \neq 0$ and $k_m = k_n$. If m corresponds to a nonpropagating mode, then $k_m = k_n^*$. This ensures that the solution to Eq. (21) is well defined and is given by

$$\begin{aligned}A_m(X_1) &= \frac{-i(f_n^{\text{surf}} + f_n^{\text{vol}})}{4P_{mn}} \left(\frac{e^{ik_n^* X_1} - e^{i2k X_1}}{k_n^* - 2k} \right) \quad \text{if } k_n^* \neq 2k \\ A_m(X_1) &= \frac{(f_n^{\text{surf}} + f_n^{\text{vol}})}{4P_{mn}} X_1 \quad \text{if } k_n^* = 2k.\end{aligned}\quad (23)$$

Note that if the primary mode is a propagating mode, and if there exists another propagating mode $n = m$ such that $k_n^* = k_n = 2k$, then the amplitude A_m increases linearly with the propagation distance and is termed as a cumulative second harmonic. While this condition is satisfied at every frequency for bulk waves, only specific primary guided wave modes generate cumulative second harmonics. The two “internal resonance” conditions that a primary mode needs to satisfy for it to generate a cumulative second harmonic are¹⁹

1. Phase-matching condition: existence of a propagating guided wave mode at $(2\omega, 2k)$, where (ω, k) is the primary mode.
2. Nonzero power-flux criterion: $(f_n^{\text{surf}} + f_n^{\text{vol}}) \neq 0$ for that mode n such that $k_n^* = k_n = 2k$.

The above analysis does not assume the nature of the primary mode and can be applied to both RL and SH modes. To identify the guided wave modes that satisfy both the conditions, one needs to analyze each of them separately as outlined below.

- Phase-matching condition^{19,23–26}

The phase-matching condition is satisfied if and only if there exists a propagating guided wave mode in the plate at $(2\omega, 2k)$, where (ω, k) corresponds to the frequency and wavenumber of the primary mode. To proceed with the analysis, we first start with the following dispersion relations

$$\begin{aligned} \frac{\tan(qh)}{\tan(ph)} &= -\frac{4k^2 pq}{(q^2 - k^2)^2} \quad (\text{symmetric RL modes}), \\ \frac{\tan(qh)}{\tan(ph)} &= -\frac{(q^2 - k^2)^2}{4k^2 pq} \quad (\text{antisymmetric RL modes}), \\ qh &= \frac{n\pi}{2} \quad (\text{shear - horizontal modes}). \end{aligned} \quad (24)$$

Here, $p = \sqrt{(\omega/c_l)^2 - k^2}$ and $q = \sqrt{(\omega/c_t)^2 - k^2}$, where c_l and c_t are the longitudinal and transverse wave speeds in the material, respectively. The phase matching condition needs to be analyzed for different combinations of primary and secondary modes. First, consider the case of a primary RL mode generating a secondary RL mode. If both the primary (ω, k) and secondary modes $(2\omega, 2k)$ are symmetric modes then we have

$$\begin{aligned} \frac{\tan(qh)}{\tan(ph)} &= -\frac{4k^2 pq}{(q^2 - k^2)^2}, \\ \frac{\tan(2qh)}{\tan(2ph)} &= -\frac{4(2k)^2 (2p)(2q)}{[(2q)^2 - (2k)^2]^2}, \end{aligned}$$

where the first one is the dispersion relation for the primary mode and the second one is the dispersion relation for the secondary mode. One interesting observation that needs to be made with regard to the above relations is that the right hand sides of both of the equations are identical which enables one to write

$$\frac{\tan(qh)}{\tan(ph)} = \frac{\tan(2qh)}{\tan(2ph)}.$$

Likewise, we can write relations for all possible combinations of the primary and secondary RL modes as follows:

$$\frac{\tan(qh)}{\tan(ph)} = \frac{\tan(2qh)}{\tan(2ph)}$$

Primary symmetric (antisymmetric)

→ Secondary symmetric (antisymmetric),

$$\frac{\tan(qh)}{\tan(ph)} = \frac{\tan(2ph)}{\tan(2qh)}$$

Primary symmetric (antisymmetric)

→ Secondary antisymmetric (symmetric).

(25)

The first relation in Eq. (25) describes a primary mode generating a secondary mode of the same kind and the second relation describes a primary mode generating a secondary mode of the opposite kind. Similar relations can be written down for a primary SH mode generating a secondary RL mode. Care must be taken in interpreting the above relations, especially when any of the terms in the equation are 0 or ∞ . A detailed analysis of the phase-matching condition can be found in Refs. 23 and 24. Next, we analyze the nonzero-power-flux criterion.

- Nonzero power flux criterion^{19,22,25–27}

To analyze nonzero power flux criterion, we adopt a parity analysis in terms of the displacement gradient (**H**). First, we begin by observing that the displacement field and the corresponding displacement gradient in the plate for different modes are of the following form given in Table 1. Here, S denotes a symmetric (even) function about the midplane of the plate and A denotes an antisymmetric (odd) function about the midplane of the plate.

Table 1 Parity of the displacement and displacement gradient for different primary modes.

Primary mode	\mathbf{u}_1 (displacement)	\mathbf{H}_1 (displacement gradient)
RL symmetric	$\begin{pmatrix} S \\ A \\ 0 \end{pmatrix}$	$\begin{bmatrix} S & A & 0 \\ A & S & 0 \\ 0 & 0 & 0 \end{bmatrix}$
RL antisymmetric	$\begin{pmatrix} A \\ S \\ 0 \end{pmatrix}$	$\begin{bmatrix} A & S & 0 \\ S & A & 0 \\ 0 & 0 & 0 \end{bmatrix}$
SH symmetric	$\begin{pmatrix} 0 \\ 0 \\ S \end{pmatrix}$	$\begin{bmatrix} S & A & 0 \\ A & S & 0 \\ 0 & 0 & 0 \end{bmatrix}$
SH antisymmetric	$\begin{pmatrix} S \\ A \\ 0 \end{pmatrix}$	$\begin{bmatrix} A & S & 0 \\ S & A & 0 \\ 0 & 0 & 0 \end{bmatrix}$

Table 2 Parity of the $\mathbf{S}^{\text{NL}}(\mathbf{H}_1, \mathbf{H}_1, 2)$ and $\text{Div}[\mathbf{S}^{\text{NL}}(\mathbf{H}_1, \mathbf{H}_1, 2)]$.

Primary mode	$\mathbf{S}^{\text{NL}}(\mathbf{H}_1, \mathbf{H}_1, 2)$	$\text{Div}[\mathbf{S}^{\text{NL}}(\mathbf{H}_1, \mathbf{H}_1, 2)]$
RL symmetric or RL antisymmetric	$\begin{bmatrix} S & A & 0 \\ A & S & 0 \\ 0 & 0 & 0 \end{bmatrix}$	$\begin{bmatrix} S & A & 0 \\ A & S & 0 \\ 0 & 0 & 0 \end{bmatrix}$
SH symmetric or SH antisymmetric	$\begin{bmatrix} S & A & 0 \\ A & S & 0 \\ 0 & 0 & 0 \end{bmatrix}$	$\begin{bmatrix} S & A & 0 \\ A & S & 0 \\ 0 & 0 & 0 \end{bmatrix}$

Correspondingly, one can show^{22,25} that the nonlinear terms $\mathbf{S}^{\text{NL}}(\mathbf{H}_1, \mathbf{H}_1, 2)$ and $\text{Div}[\mathbf{S}^{\text{NL}}(\mathbf{H}_1, \mathbf{H}_1, 2)]$ are of the parity indicated in Table 2.

From the above observations, one can conclude²⁶ the following:

- $f_n^{\text{surf}} = (1/2)\mathbf{S}^{\text{NL}}(\mathbf{H}_1, \mathbf{H}_1, 2)\mathbf{v}_n^* \cdot \mathbf{n}_2|_{-h}^h \neq 0$ if and only if \mathbf{v}_n corresponds to a symmetric mode.
- $f_n^{\text{vol}} = (1/2)\int_{-h}^h \text{Div}[\mathbf{S}^{\text{NL}}(\mathbf{H}_1, \mathbf{H}_1, 2)] \cdot \mathbf{v}_n^* dX_2 \neq 0$ if and only if \mathbf{v}_n corresponds to a symmetric mode.

Therefore, the power-flux $f_n^{\text{surf}} + f_n^{\text{vol}} \neq 0$ if and only if the secondary mode is a symmetric RL mode. It should be noted that this would also be the case even if the primary mode is an SH mode.²⁶

From the conclusions obtained for both the phase-matching and nonzero power flux criteria, one can identify the following list (Table 3) of guided wave modes that are capable of generating cumulative second harmonics. Here, m, n denote arbitrary positive integers. In addition to the modes listed in Table 3, other modes²⁵ like the quasi-Rayleigh modes and (high-frequency) guided wave modes near the transverse wave speeds are also capable of second-harmonic generation.

2.3 Mode Selection

The importance of selecting a primary mode that generates a higher harmonic with strong internal resonance was mentioned in Sec. 1, but it cannot be overemphasized. Internal resonance is the first consideration; starting with phase matching and then assessing the secondary modes that have not just nonzero power flux, but significant power fluxes.²⁸ Other important considerations include: modal excitability given the selected transducer, proximity of nearby modes, dispersion, diffraction, and attenuation. In fact, the number of primary modes that generate internally resonant second

harmonics that are measured by currently available transducers are so low that the generation of third harmonics was analyzed.²⁹

2.4 Nonlinear Guided Waves in Other Waveguides

In this section, we briefly summarize some of the earlier work concerning nonlinear guided waves in nonplate-like waveguides. Second harmonic, sum, and difference frequency generation in waveguides of arbitrary cross section was first investigated by De Lima and Hamilton.³⁰ The conditions for internal resonance were arrived at and also second-harmonic generation in cylindrical rods and shells was numerically demonstrated. Likewise, generalized higher harmonic generation in waveguides of arbitrary cross section was investigated.^{31,32} Second-harmonic guided waves from axis-symmetric longitudinal modes in pipes were investigated in Ref. 33 using a large-radius asymptotic approximation for wavestructures in pipes. Limits on the thickness to diameter ratio were discussed by Chillara and Lissenden.³³ It was observed that these wavestructures for pipes converge asymptotically to that of plates, hence, conclusions concerning second-harmonic generation for plates can be appropriately extended for pipes. Second-harmonic generation from axis-symmetric torsional and longitudinal modes was analyzed in Ref. 34. Recently, higher order mode interactions in pipes were studied^{35,36} where harmonic generation from flexural modes was analyzed as well.

3 Numerical Simulations

In this section, we discuss numerical simulations pertaining to nonlinear guided wave propagation in waveguides. Numerical simulations offer a convenient way to investigate the cumulative harmonic generation in waveguides and offer key insights into aspects of guided wave mode selection for efficient harmonic generation from a practical standpoint. The numerical studies enable us to alienate the nonlinear effects arising out of instrumentation and just study the effect of material nonlinearity on the wave propagation. Both semianalytical and numerical methods have successfully been employed to investigate nonlinear guided waves in waveguides.

Nucera and Lanza di Scalea³⁷ developed a COMSOL based nonlinear semianalytical finite element (CO.NO. SAFE) to analyze synchronism conditions for mode-selection and also to determine the modal amplitude content at second harmonics in waveguides. The method was demonstrated for variety of waveguides like rail, composite laminates, reinforced concrete slab, and so on. Finite-difference-time-domain method incorporating material and geometric

Table 3 List of guided wave modes that can generate cumulative second harmonics.

Primary mode	Cut-off modes	$c_p = c_l$	$c_p = \sqrt{2}c_t$	Mode-intersections	Special modes
RL symmetric (ω)	$\frac{n\pi c_l}{h}$	$\frac{n\pi c_l c_t}{h\sqrt{c_l^2 - c_t^2}}$	$\frac{\sqrt{2}n\pi c_l c_t}{h\sqrt{2c_l^2 - c_t^2}}$	All	—
RL antisymmetric (ω)	$\frac{(2n+1)\pi c_l}{2h}$	—	$\frac{\sqrt{2}n\pi c_l c_t}{h\sqrt{2c_l^2 - c_t^2}}$	All	—
SH (ω)	$\frac{n\pi c_l}{2h}$	$\frac{n\pi c_l c_t}{2h\sqrt{c_l^2 - c_t^2}}$	—	—	Modes that satisfy $\left(\frac{1}{c_l^2} - \frac{1}{c_p^2}\right) = \frac{n^2}{h^2} \left(\frac{1}{c_l^2} - \frac{1}{c_p^2}\right)$

Table 4 Elastic constants in GPa used for simulations.

λ	μ	l	m	n
51	26	-250	-333	-350

nonlinearities was employed³⁸ to study center-frequency dependence of cumulative harmonic generation in isotropic plates. Likewise, two local approaches, namely cellular automata finite element and local interaction simulation approach have been employed³⁹ to study second-harmonic guided wave generation in waveguides. On the other hand, conventional finite element methods incorporating material and geometric nonlinearities were extensively used^{26,28,36,40-42} to study second-harmonic guided wave propagation in waveguides, especially in plates and pipes. In this section, we discuss the results from finite element simulations concerning second-harmonic guided waves in plates. First, we discuss second-harmonic guided wave generation in homogeneous, isotropic plates in Sec. 3.1, and then discuss results for second-harmonic guided waves in plates with inhomogeneous/localized nonlinearities in Sec. 3.2.

3.1 Second-Harmonic Guided Waves in Homogeneous Isotropic Plates

All the results presented in this section are obtained using the commercial finite element software COMSOL. Results are presented for an aluminum plate (1-mm thick) whose material properties are shown in Table 4. Figure 2 shows the schematic of the model used for simulations. The wave excitation is specified as a displacement boundary condition at $x = 0$ to excite the appropriate mode. Throughout this section, we denote the x -component of the displacement with “ u ” and the y -component of the displacement with “ v .” Figure 3 shows the dispersion curves for the plate along with the primary modes used for the study in red.

3.1.1 Cumulative versus noncumulative second-harmonic generation

Here, we discuss and compare the second-harmonic generation from two different primary modes; S_0 mode (0.5 MHz) and the S_1 mode (3.6 MHz). For the FE discretization, triangular plane-strain elements with a maximum size of 0.1 mm are employed to discretize the domain along the wave propagation direction and a minimum of 15 elements are used along the thickness direction. A maximum time-step of $0.01 \mu\text{s}$ is used for the S_0 mode and $0.005 \mu\text{s}$ is used for the S_1 mode. Displacement amplitudes of 1×10^{-7} m and 2×10^{-8} m are used for the boundary conditions for the S_0 mode and the S_1 mode, respectively. This choice ensures a stress wave of a few MPa—typical of an ultrasonic wave propagating in the material. Note while the S_1 mode (3.6 MHz) satisfies the conditions of internal resonance

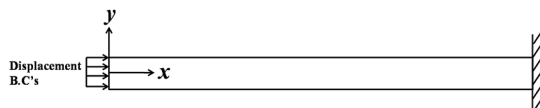


Fig. 2 Schematic of the model used for simulations.

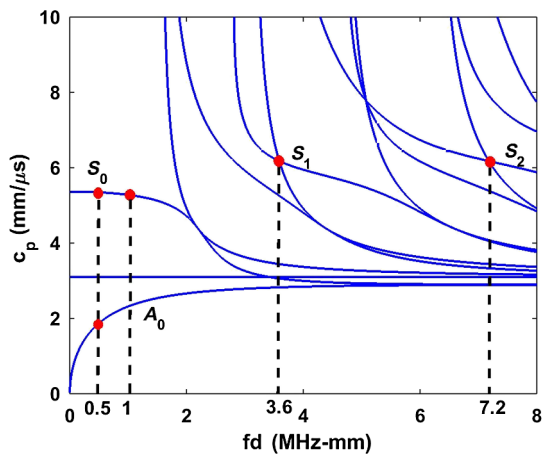


Fig. 3 Dispersion curves for the aluminum plate showing the primary and secondary modes in the simulations.

discussed in Sec. 2.2, while the S_0 mode (0.5 MHz) does not satisfy the phase matching criterion of Sec. 2.2. The phase velocity of the primary S_0 mode (0.5 MHz) is $5.34 \text{ mm}/\mu\text{s}$ and that of the second harmonic S_0 mode (1 MHz) is $5.27 \text{ mm}/\mu\text{s}$. On the other hand, the phase velocity of both the primary S_1 mode (3.6 MHz) and the secondary S_2 mode (7.2 MHz) is $6.17 \text{ mm}/\mu\text{s}$.

Figure 4 shows the amplitude of the second harmonic from the S_0 mode (0.5 MHz) and Fig. 5 shows the same for the S_1 mode (3.6 MHz) as a function of the normalized propagating distance. The normalization is carried out using the corresponding wavelength of the primary mode ($\lambda_{S_0} = 10.68 \text{ mm}$, $\lambda_{S_1} = 1.71 \text{ mm}$). Clearly, the second harmonic from the S_0 mode (0.5 MHz) is not cumulative as it starts to decrease after about $((x/\lambda_{S_0}) = 10)$. On the other hand, the second harmonic from the S_1 mode (3.6 MHz) is cumulative and increases linearly as shown in Fig. 5. This is in agreement with the prediction from the perturbation approach presented in Sec. 2.2 that the S_1 mode (3.6 MHz) generates a cumulative second harmonic.

3.1.2 Role of material and geometric nonlinearities

In this section, we compare the contribution of material and geometric nonlinearity to the second-harmonic generation. Simulations are carried out for the primary S_1 mode

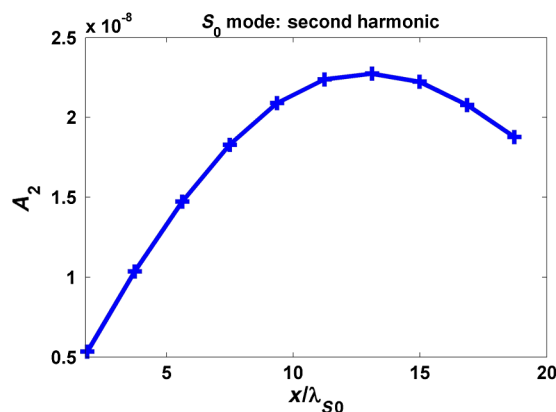


Fig. 4 Second-harmonic amplitude (A_2 in m) from primary S_0 mode (0.5 MHz) with normalized propagation distance.

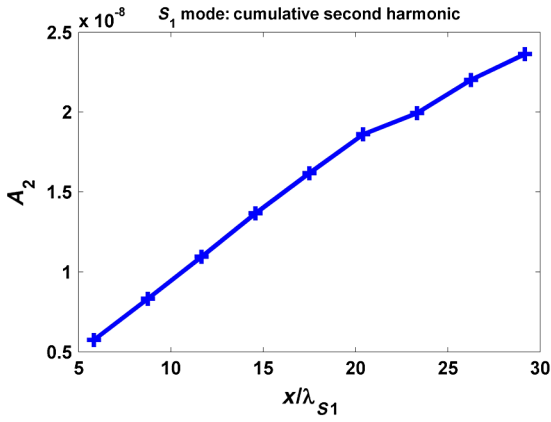


Fig. 5 Second-harmonic amplitude (A_2 in m) from primary S_1 mode (3.6 MHz) with normalized propagation distance.

(3.6 MHz) generating a second-harmonic S_2 mode (7.2 MHz) for three variants of the constitutive model in Eq. (6). These are:

1. Linear elastic material (LE)—no material or geometric nonlinearities are included, i.e., $l = m = n = 0$ [Eq. (6)] and linearized strain, $\mathbf{E}_{lin} = (1/2)(\mathbf{H} + \mathbf{H}^T)$ is used as a strain measure.
2. Nonlinear (NL)—both material and geometric nonlinearities are included, i.e., $l \neq 0, m \neq 0, n \neq 0$ (values from Table 1) and Lagrangian strain (\mathbf{E}) is used as a strain measure.
3. Geometrically nonlinear (NG)—only geometric nonlinearity is included, i.e., $l = m = n = 0$ and Lagrangian strain (\mathbf{E}) is used as a strain measure.

Figure 6 shows fast Fourier transforms for LE, NL, and NG cases at $x = 50$ mm from the left end of the plate. Clearly, the NL case has a much higher second harmonic and is about 10 times that for the NG case. The results presented here indicate that the second-harmonic generation is dominated by the material nonlinearity as opposed to the geometric nonlinearity. Hence, it can be concluded that geometrically linear theories incorporating material nonlinearity

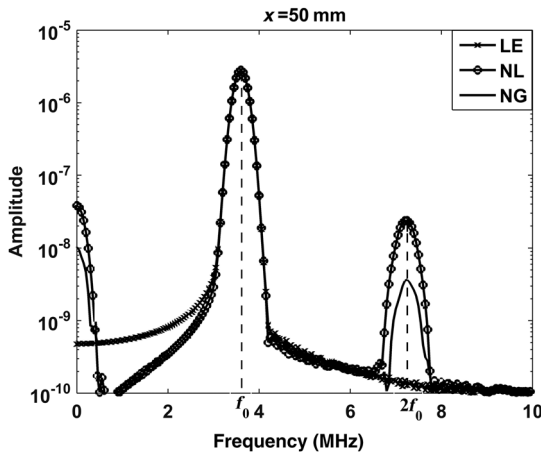


Fig. 6 Primary mode: S_1 mode (3.6 MHz)—fast Fourier transforms (log-scale) obtained from time domain signals at $x = 50$ mm for the three cases: linear elastic material, nonlinear, and geometrically nonlinear.

for material behavior provide a very good approximation for studying nonlinear guided waves in plates.

3.1.3 Second-harmonic generation with group velocity mismatch

The results presented in the previous sections considered primary modes that are (almost) phase-matched to their second harmonic. To investigate the effect of group velocity mismatch on the second-harmonic generation, simulations are run for the primary A_0 mode (0.5 MHz). The amplitude of the displacement boundary condition is increased to 10^{-5} m to decipher some important aspects of second-harmonic generation as outlined later. Figure 7 shows the Hilbert transform (positive envelope) of the time-domain signals on a log-scale at $x = 40, 80,$ and 120 mm from the left end of the plate. Clearly, there are two distinct peaks corresponding to the arrival time of the pulses; the one with a larger amplitude corresponds to the primary mode and arrives later due to a smaller group velocity (2.91 mm/ μ s), and the smaller one corresponds to the secondary mode and arrives earlier in time due to a larger group velocity (5.12 mm/ μ s). Also, they are clearly separated with the time-difference between them increasing with increasing propagation distance. A few important observations can be made in this regard:

1. The second harmonic separates from the primary mode, the hence group velocity matching is not required for the higher harmonic generation. Note that the phase matching condition is not satisfied here. This finding, which is explained further in Ref. 40, is in direct conflict with the reasonable argument presented by Muller et al.²⁵ that the primary and secondary wave packets must travel together in order for energy transfer to occur. Our explanation is that the higher harmonic is generated by the material nonlinearity with the nonlinear surface traction f_n^{surf} and nonlinear body force f_n^{vol} terms [Eq. (22)] acting like distributed sources in a similar way that parametric arrays use distributed nonlinearity in fluids to generate directional sound beams. Thus, we believe it is the material's nonlinearity itself that enables the secondary wave packet to propagate and be cumulative when the internal resonance criteria are satisfied.

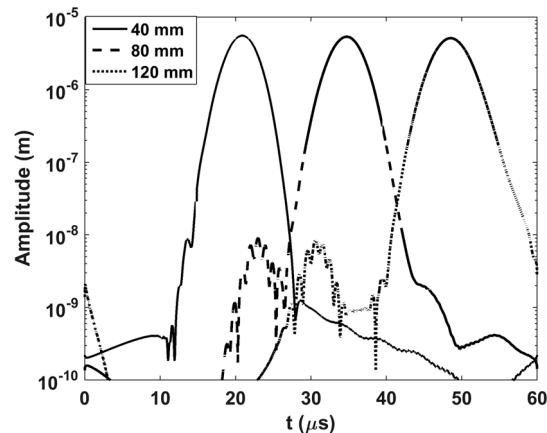


Fig. 7 Primary mode: A_0 mode (0.5 MHz)—Hilbert transform of time domain signals at $x = 40, 80,$ and 120 mm.

However, if the primary and secondary waves have different group velocities, due care must be taken in their measurement.

2. The second-harmonic mode generated is the S_0 mode (1 MHz) as opposed to the A_0 mode (1 MHz) as is evident from the through-thickness displacement profiles “ v ” in Fig. 8 at $x = 120$ mm during the times $t = 28$ to $35 \mu\text{s}$, which is antisymmetric about the mid-plane. This is in agreement with the predictions from the perturbation approach.
3. It can be concluded that the second harmonic is continuously generated from the primary mode and once generated, it can propagate independent of the primary mode. This can be explained with the following rationale. As observed here, the second harmonic separates from the primary mode and propagates as a distinct pulse independent of the primary mode. Now, the residual primary mode can again generate a second harmonic and this process repeats with the second-harmonic pulses being separated from the primary mode when sufficient time has elapsed—as dictated by the group velocity mismatch between the primary and the secondary modes. Also, the separated harmonic can itself generate other higher harmonics. The theory of mode interaction presented in Ref. 22 can be used to assess the nature of such a higher harmonic generation. It should be noted that these are much smaller in magnitude when compared to the primary mode and pose an enhanced difficulty in detecting them in an experiment.

3.2 Second-Harmonic Guided Waves in Plates with Inhomogeneous/Localized Nonlinearities

3.2.1 Homogeneous versus inhomogeneous nonlinearity

Here, we compare the cumulative second-harmonic generation characteristics from S_1 mode (3.6 MHz) for two cases, namely homogeneous and nonhomogeneous nonlinearities in the plate. For the homogeneous case, the Murnaghan constants from Table 4 were used. For the nonhomogeneous

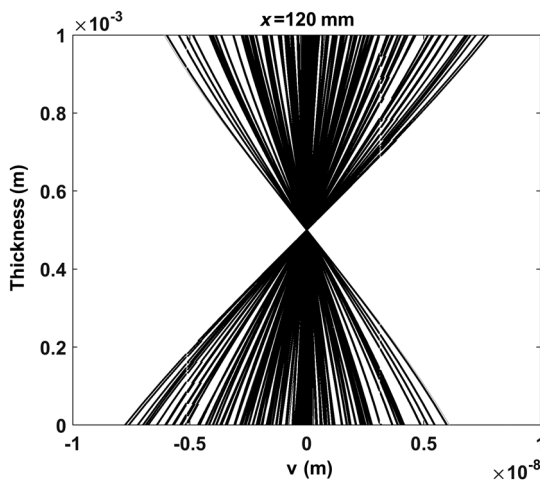


Fig. 8 Primary mode: A_0 mode (0.5 MHz)—through thickness “ v ” displacement profiles at $x = 120$ mm and $t = 28$ to $35 \mu\text{s}$ indicate the S_0 mode.

case, the parameters λ and μ in Table 4 were used and the Murnaghan constants were varied along the wave propagation direction (x). The variation is assumed to be linear, such as for a functionally graded material i.e., $l(x) = -250(1 + x/25)$ GPa, $m(x) = -333(1 + x/25)$ GPa, and $n(x) = -350(1 + x/25)$ GPa, where “ x ” is in “mm” so that the Murnaghan constants at $x = 50$ mm are three times those at $x = 0$ mm. Figure 9 shows the amplitude of the second harmonic with normalized propagation distance. Clearly, the amplitude of the second harmonic for the inhomogeneous case is much higher due to the higher nonlinearity. Also, it should be noted that the cumulative second-harmonic generation is not linear (but super-linear) as for the homogeneous case.

3.2.2 Effect of localized through-thickness nonlinearity on cumulative second-harmonic generation

In Sec. 3.2.1, we investigated the effect of inhomogeneous nonlinearity along the wave propagation direction. Now, we investigate the effect of localized through-thickness nonlinearity on the second-harmonic generation of guided waves, such as may be the case in a one-sided degradation process. Simulations are run for two primary modes, namely, the S_0 mode (0.5 MHz) and the S_1 mode (3.6 MHz). Localized nonlinearity in the model is obtained by varying the percentage through-thickness nonlinearity as indicated in the Fig. 10, where “LE” denotes LE and “NL” denotes nonlinear elastic material. The results presented in this section are from Ref. 41.

S_0 mode (0.5 MHz). We first present the results obtained for second-harmonic generation from the S_0 mode at 0.5 MHz. Figure 11 shows the relative nonlinearity parameter (A_2/A_1^2) at $x = 100$ mm versus the percentage through-thickness of nonlinearity. Clearly, it increases linearly with the amount of through-thickness nonlinearity. Also, Fig. 12 shows the relative nonlinearity parameter as a function of the propagating distance for varying levels of through-thickness nonlinearity. As can be seen, the nonlinearity parameter increases with the propagation distance for each of the cases. Moreover, the rate of increase of the nonlinearity parameter increases with increasing through-thickness nonlinearity.

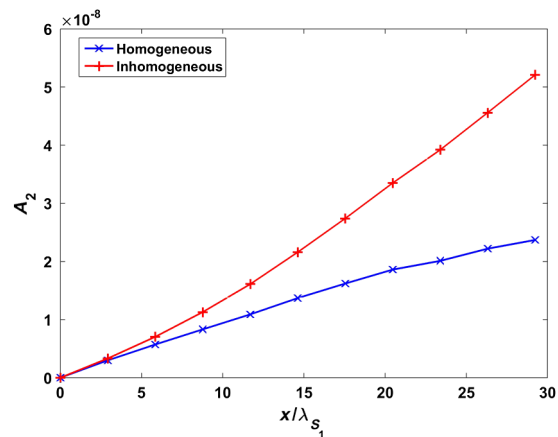


Fig. 9 Primary mode: S_1 mode (3.6 MHz)—comparison of the second-harmonic amplitude (A_2 in m) for homogeneous and inhomogeneous nonlinearity distribution.

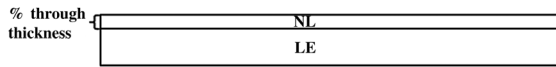


Fig. 10 Schematic of the model with through-thickness nonlinearity used for the simulation.

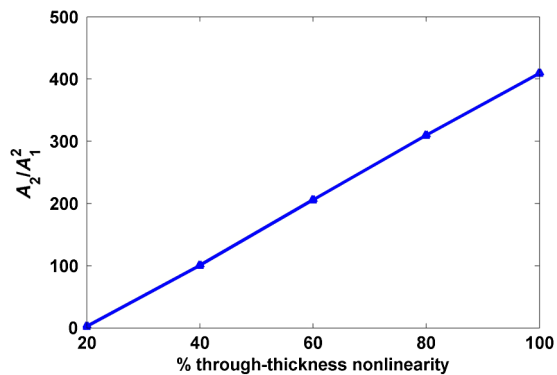


Fig. 11 Relative nonlinearity parameter versus the percent through-thickness nonlinearity.

Also, it should be noted that the 20%–20% case which corresponds to 20% nonlinearity on the top and 20% nonlinearity on the bottom of the plate almost coincides with the case with 40% nonlinearity on the top. Hence, it appears that the second-harmonic generation from the S_0 mode (0.5 MHz) is independent of the through-thickness damage location, but only depends on the volume-fraction of the nonlinear material. This is clearly evident from the plots of the normalized relative nonlinearity parameter shown in Fig. 13 where each curve is normalized with its value at $x = 20$ mm and all of them except one (20%) coincide. This is because, for the 20% case, the energy from the primary mode is transferred to the antisymmetric mode at the second harmonic in addition to the symmetric mode. This occurs due to the asymmetry of the material parameters in the top and bottom surfaces of the plate in Fig. 10.

It should be noted that the second-harmonic generation from the S_0 mode (0.5 MHz) is independent of the location of the damage due to its uniform wavestructure through the thickness as indicated in Fig. 14.

Next, we present the results obtained for second-harmonic generation from the S_1 mode at 3.6 MHz.

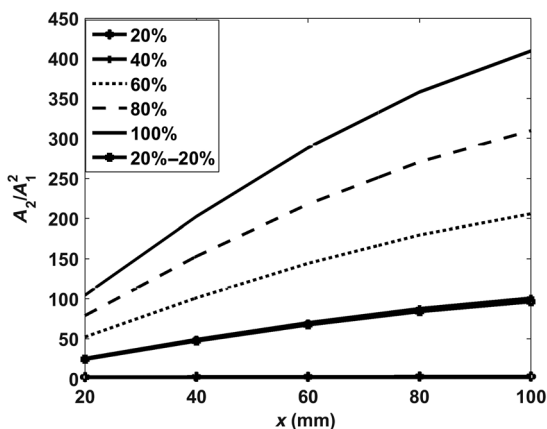


Fig. 12 Relative nonlinearity parameter versus the propagation distance for different levels of through-thickness nonlinearity.

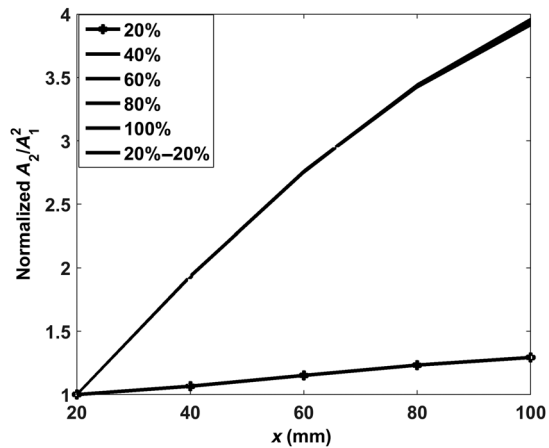


Fig. 13 Normalized relative nonlinearity parameter versus the percent through-thickness nonlinearity.

S_1 mode (3.6 MHz). Simulations similar to the one for the S_0 mode (0.5 MHz) are run for the S_1 mode (3.6 MHz) by varying the through-thickness nonlinearity in the plate. Simulations were run for different cases of through-thickness nonlinearity, namely, 20%, 40%, 60%, 80%, 90%, 100%, and 20%–20%, which again corresponds to 20% through-thickness damage on the top and 20% on the bottom. Unlike the S_0 mode (0.5 MHz), the wavestructure for the S_1 mode is not uniform through the thickness as indicated in the Fig. 15, which depicts the wavestructures of both the S_1 mode (3.6 MHz) and the S_2 mode (7.2 MHz). Hence, we expect the results to be different from those obtained for the S_0 mode (0.5 MHz).

Figure 16 shows the relative nonlinearity parameter as a function of the propagation distance. Several observations are made in this regard.

1. Relative nonlinearity parameter is much higher when compared to that from the S_0 mode (0.5 MHz) due to the higher frequency and cumulative nature of the S_1 mode (3.6 MHz).
2. Relative nonlinearity parameter is not monotonic with the increasing volume-fraction of the through-thickness damage. Hence, it can be concluded that the second-harmonic generation from the S_1 mode (3.6 MHz)

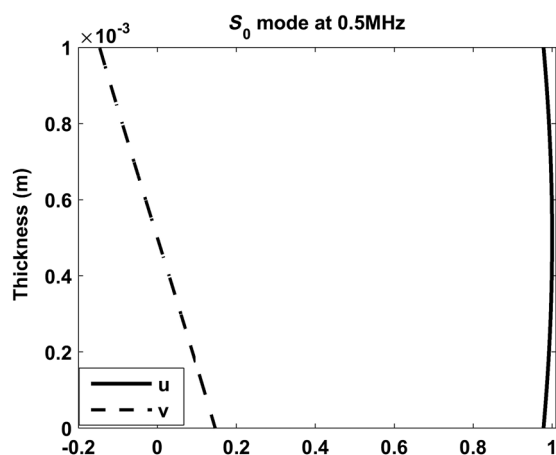


Fig. 14 S_0 mode (0.5 MHz)-wavestructure.

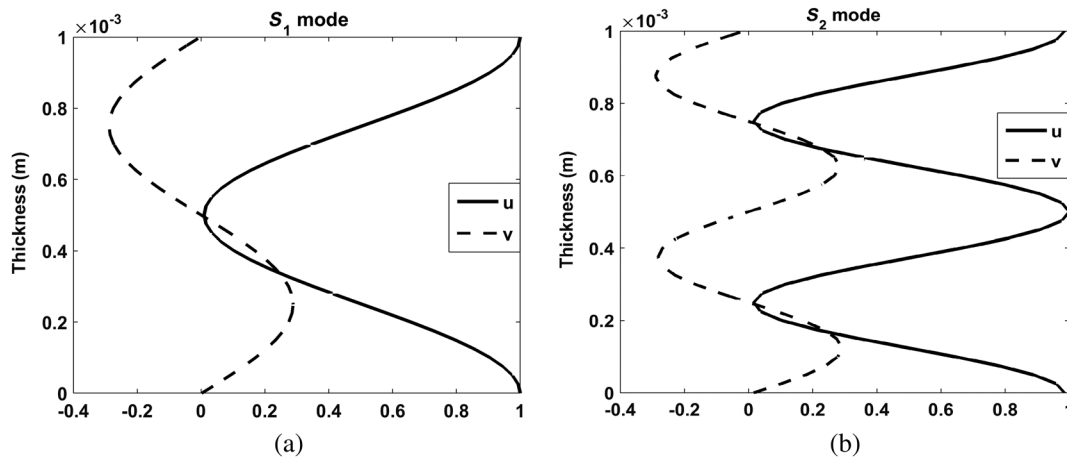


Fig. 15 Wavestructures: (a) S_1 mode (3.6 MHz) and (b) S_2 mode (7.2 MHz).

is not exclusively dependent on the volume fraction of through-thickness nonlinearity.

3. The case of 20%–20% coincides with that for 100%, hence it can be concluded that the second-harmonic generation is mainly due to the contribution from the material near the surface rather than that from the central portion (bulk) of the plate. In fact, it appears that the bulk contribution reduces the second-harmonic generation a little as is evident from Fig. 16 where the 20%–20% case surpasses the 100% for $x > 30$ mm.

From the above study, it appears that the second-harmonic generation from the $S_1 - S_2$ mode pair at the longitudinal wave speed is more sensitive to the surface damage and can be used to efficiently detect and characterize it.

4 Experiments

Naturally, experiments are a vital part of the development of nonlinear ultrasonic guided wave-based techniques for characterization of material microstructure evolution. Even more so than for linear ultrasonic guided waves, the probability of successful experiments is low unless the nonlinear guided wave propagation characteristics are understood and used to select modes, frequencies, and transducers that activate primary waves that, in turn, generate strong cumulative higher harmonics. This section starts by describing general

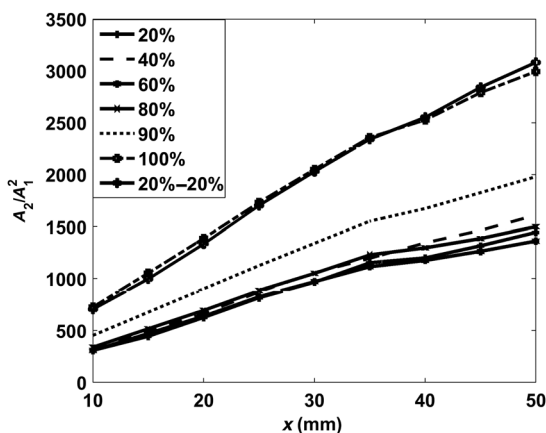


Fig. 16 Cumulative second harmonic from the S_1 mode (0.5 MHz) for varying levels of through-thickness damage.

considerations for nonlinear ultrasonic guided wave experiments intended to measure the generation of higher harmonics. It then reviews experimental results that have been reported in the literature.

4.1 Measurement Considerations

The first and foremost experimental consideration is that a finite amplitude near-monochromatic waveform having excellent clarity is actuated. Three issues are embedded in this consideration: (1) finite amplitude is desirable in order that the generated higher harmonics, which have far less energy than the primary wave, are measurable; (2) the tail of the frequency distribution can overwhelm the higher harmonics unless a narrow bandwidth excitation is obtained, thus a toneburst excitation having a large number of cycles is typical; and (3) high-signal clarity, or lack of distortion, reduces the noise in the frequency spectrum making the very low amplitude higher harmonics generated by the material more evident. These issues apply to bulk waves and guided waves, but because guided waves are multimodal, it is even more important to get as much energy as possible into the selected primary wave mode at the frequency that will generate the higher harmonic of interest. The second consideration, which is linked to the first, is the intrinsic nonlinearity of the measurement system. A typical measurement system comprises: synthesizer, amplifier, cables, transmit transducer, coupling media, test material, more coupling media, receive transducer, cabling, preamplifier, and oscilloscope. Matching networks and filters are also often used to improve system performance. It is important that the signal distortion due to the material nonlinearity dominates the distortion associated with other elements in the measurement system. The considerations described above are always a concern, but specific experimental setups will have additional considerations. For example, the ability to separate the transmitter and receiver by different distances enables the cumulative nature of higher harmonic waves to be assessed. Hence, it provides confirmation that the distortion causing higher harmonic generation is associated with the material.

4.2 Transducers

Once a primary mode and the higher harmonic that it generates have been selected, transducers can be chosen to

transmit and receive based on mode excitability. The wave-structure (i.e., transverse resonance pattern) for the selected primary mode and frequency dictates the effectiveness of a transducer to actuate that mode. The proximity of other modes to the frequency/wavenumber of the selected mode and their excitability dictates how preferentially the selected primary mode is actuated with respect to the other modes. Similar considerations apply to receiving the higher harmonic mode. Waves actuated from finite-size transmitters will diffract, which was not modeled in Sec. 2. Material attenuation was not modeled either, thus the linear cumulative effect of higher harmonics given by Eq. (22) for internally resonant mode pairs is not attained due to diffraction and attenuation. Note that internal resonance is not required for higher harmonic generation, but it is required for the higher harmonic to be cumulative. Preferred transmitters have a large footprint to minimize diffraction, strong coupling between the electrical signal and resulting mechanical disturbance, and minimal distortion of the waveform. Many researchers choose to minimize distortion at the expense of strong coupling by choosing single crystal lithium niobate instead of polycrystalline lead zirconate titanate (PZT) for piezoelectric transducers. Preferential excitation of guided wave modes can be achieved with angle beam transducers and comb (or interdigital) transducers regardless of the type of transduction. The means of coupling the transmitter to the material is important because conventional gel couplant exhibits significant nonlinearity relative to solid media. On the receiving side, the preferred transducer is broadband so that it can receive both the primary and the higher harmonic frequencies without bias, but this is often not practical.

4.3 Description of Nonlinearity

Most studies of second-harmonic generation employ some version of the nonlinearity coefficient β to describe the material nonlinearity. In solids, β is often called the acoustic nonlinearity parameter, much to the chagrin of the nonlinear acoustics community. The use of β for nonlinearity in solid media originates with lossless bulk longitudinal plane waves modeled in one-dimensional (1-D),⁴³ where the boundary condition $u(0, t) = u_o \cos \omega t$ results in

$$u(x, t) = \frac{\beta}{8} (ku_0)^2 x + u_o \cos(kx - t) - \frac{\beta}{8} (ku_0)^2 x \cos[2(kx - \omega t)],$$

so clearly the amplitudes of the primary wave and the second harmonic are

$$A_1 = u_o, \quad A_2 = \frac{\beta}{8} (ku_0)^2 x,$$

and the nonlinearity parameter can be written as

$$\beta = \frac{8 A_2}{k^2 x A_1^2}.$$

Thus, it is common to employ the relative nonlinearity parameter, $\beta' = (A_2/A_1^2)$. However, the propagation of guided waves is not a 1-D problem, as the transverse resonance in the waveguide creates unique displacement profiles for the displacement components. Thus, strictly speaking, β

is not applicable to guided waves. It is useful to consider the modal amplitude ratios, A_2/A_1^2 and A_3/A_1^3 , for second and third harmonics, respectively, which, of course, are the relative second and third order nonlinearity parameters. It should be emphasized that these modal amplitudes imply that A_1 is constant, i.e., there is no diffraction or attenuation, and the ratio is employed because it is often difficult to replicate the same primary wave amplitude time after time in experiments.

4.4 Metal Plates

Nonlinear RL waves in metal plates are the major subsection on experiments and this is subdivided by the type of transducer employed: angle beam, magnetostrictive, and disc.

4.4.1 Angle beam transducers

Angle beam transducers enable preferential mode activation through Snells law; i.e., the wedge angle is selected by the phase velocity of the intended mode/frequency. The first experiments on second-harmonic generation were reported by Deng et al.^{44,45} for an aluminum plate at the A_2/S_2 mode intersection point (see Table 3). Their results are shown in Fig. 17 and demonstrate both second-harmonic generation (of the S_4 mode) and its cumulative nature. We point out that the group velocities of the primary and secondary modes do not match (3.4 and 2.3 mm/ μ s).

Bermes et al.⁴⁶ then showed that the S_1 primary mode at the longitudinal wave speed ($c_p = c_l$, see Table 2) generates a cumulative S_2 second harmonic. A diffraction-based correction factor of $1/\sqrt{x}$ is employed when assessing the cumulative nature of the second harmonic. These authors used the short-time-Fourier transform to create a spectrogram onto which they superimposed the group velocity dispersion curves as shown in Fig. 18. In this case, the group velocities of the S_1 and S_2 modes are well matched (4.3 mm/ μ s). Bermes et al.⁴⁷ then expand their analysis to include the primary S_2 mode, also at $c_p = c_l$, and the S_4 secondary mode. The use of a laser interferometer to receive the wave signals has several advantages that include: flat frequency response, no averaging affects from a finite size receiver, and because it is a noncontact measurement, it is easy to change the propagation distance.^{46,47}

Matlack et al.⁴⁸ performed a comparative study of three internally resonant mode pairs ($S_1 - S_2$, $S_2 - S_4$, and $A_2/S_2 - S_4$) with the result that the $S_1 - S_2$ mode pair is preferred for practical reasons, but since the $S_2 - S_4$ mode pair has a higher β' , it would be preferred given more effective experimental procedures (i.e., it is difficult to preferentially activate the S_2 mode at $c_p = c_l$). Pruell et al.^{49,50} compared the use of an angle beam receiver with laser interferometer reception for an aluminum plate that was plastically deformed. They found that β' increased initially due to plastic deformation and then remained relatively constant. The β' values obtained from the laser interferometer were lower than those from the angle beam receiver because the piezoelectric transducer used for the angle beam was selected to preferentially receive the second-harmonic frequency, and therefore, partially filtered the primary wave. Pruell et al.⁵¹ showed that β' increases with low-cycle fatigue for the $S_1 - S_2$ mode pair. Cycling was performed in load control and the maximum plastic strain was less than 0.02 m/m after 50 cycles, which gave an increase of 17%

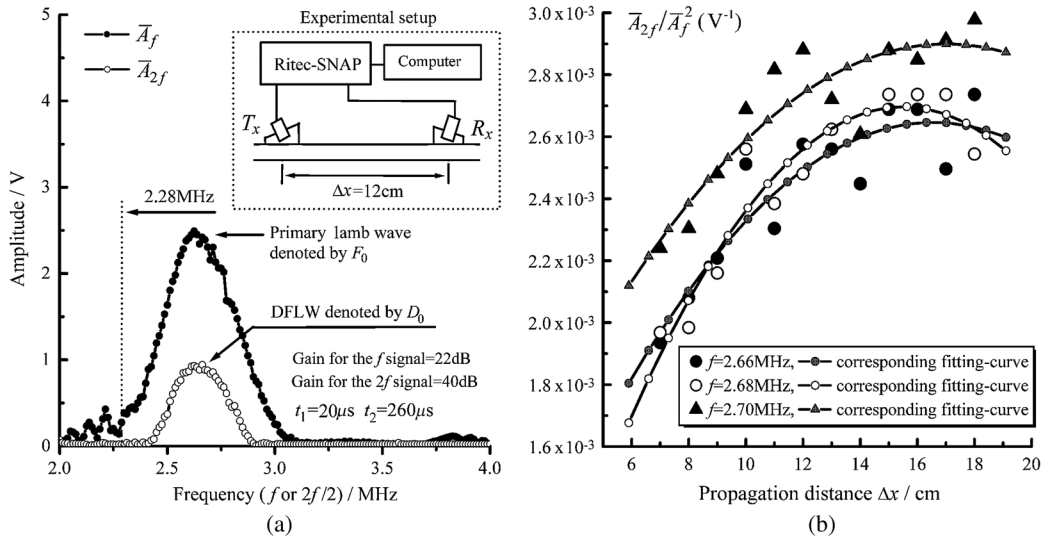


Fig. 17 (a) Primary and second harmonic amplitudes and (b) relative nonlinearity parameter with the propagation distance. (Reprinted from Ref. 44 with the permission of authors and AIP Publishing.)

in β' . From a theoretical perspective, it is surprising that Lee et al.⁵² found the $A_1 - A_2$ mode pair to give a second harmonic that increased with the propagation length. Liu et al.⁵³ compared second-harmonic measurements of anti-symmetric modes with symmetric modes and found them to be significantly smaller, but not zero.

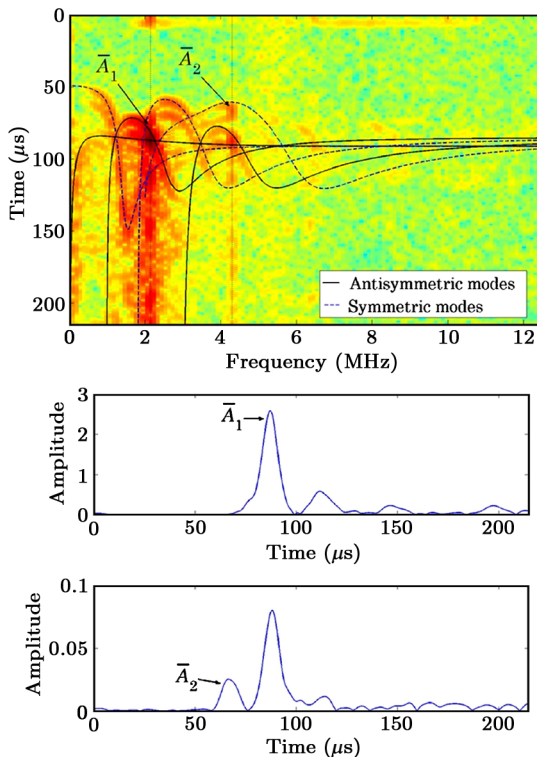


Fig. 18 Spectrogram showing the amplitudes and time of arrival of the primary and secondary modes. (Reprinted from Ref. 46 with permissions from authors and AIP Publishing.)

4.4.2 Magnetostrictive transducers

A magnetostrictive transducer (MST) consisting of a magnetostrictive (e.g., iron-cobalt) foil, a meandering electric coil, and a permanent magnet functions similar to a comb transducer, in that the coil spacing dictates the preferred wavelength. The foil is typically coupled to the plate by adhesive bonding. By orienting the permanent magnetic field bias collinear with the electric current in the coil, SH wave modes are activated/received, while orienting it perpendicular results in RL wave modes. Liu et al.²⁶ showed that the internally resonant $SH_3 - S_4$ mode pair is cumulative and detectable with MSTs. The MST transmitter was configured to send the SH_3 mode at frequency $f_0 = 2.63 \text{ MHz}$, while the MST receiver was configured to receive the S_4 RL mode at $2f_0$. Due to the finite size of the MSTs, energy was received at both the primary and second-harmonic frequencies. Energy was received at the primary frequency because the wavefront was curved, thus creating a detectable RL component from the primary SH wave. Finite element simulations were conducted to demonstrate this by investigating 20 and 100 mm wide MSTs. Lissenden et al.⁵⁴ showed that the third harmonic of the fundamental SH_0 mode is quite sensitive to plastic deformation. In this investigation, 2024-T3 aluminum plates were plastically deformed within a reduced width region having lengths of $L = 51, 102, 229, \text{ and } 457 \text{ mm}$. The wave propagation distance was 430 mm, thus the plastic strain localization increased as L decreased, even though it was reasonably uniform (i.e., 5% to 8%) over the distance L . The modal amplitude ratio, A_3/A_1^3 , was 4.8 times larger for a uniformly deformed plate than it was for an undeformed plate. As the localization increased, the A_3/A_1^3 decreased linearly until it was indistinguishable from the undeformed plate for a localization-to-propagation distance ratio of 0.12. Furthermore, the plastic strain level was shown to have a significant effect on the modal amplitude ratio, A_3/A_1^3 . In the related experiments presented by Lissenden et al.⁵⁵ using load-controlled cycling to fatigue smooth-sided plate samples, the modal amplitude ratio increased by a factor of 3.6 at 80% of the fatigue life relative to the pristine material.

No fatigue cracks were visually evident. Thus, the large change in the modal amplitude ratio has a strong potential to represent material degradation prior to initiation of a macroscale crack.

4.4.3 Disc transducers

PZT disc transducers are inexpensive and easily surface-bonded to take advantage of the shear stress activated in the adhesive associated with radial resonance of the disc. However, mode control capabilities are very limited. Hong et al.⁵⁶ reported β' for a pristine aluminum plate that appears to increase linearly with propagation distance. However, the PZT disc actuator actuates a circular crested wave whose primary amplitude decreases as $1/\sqrt{r}$ with propagation distance, so it is likely that the results are significantly affected by the primary wavefront spreading. Hong et al.⁵⁶ also investigated the effect of a small fatigue crack on β' with PZT discs and finite element modeling that includes material nonlinearity as well as contact acoustic nonlinearity (CAN) from opening and closing of the crack. The authors plotted β' as a function of distance from the crack as shown in Fig. 10 of Hong et al.⁵⁶ In the experiment, a 4-mm long high-cycle fatigue crack half way through the thickness of the plate was initiated in a single edge notch sample. Material plasticity associated with dislocation dipoles was included in the model, but since the authors do not discuss the plastic zone size, it is implied that the material is modeled as being homogeneous. If this is, indeed, the case, then the results indicate that the CAN dominates the material nonlinearity, otherwise β' would not have decreased for wave paths located further from the crack. Hong et al.⁵⁷ use second harmonics for imaging fatigue damage at a rivet hole by using an array of disc transducers.

We note that CAN associated with breathing cracks has been studied by numerous researchers using sub- and super-harmonic generation methods.^{58–61}

4.5 Other Waveguides (Composite Plate, Pipes, Rods, and Rail)

While the majority of the nonlinear guided wave experiments were conducted on metal plates, other nondestructive evaluation applications of note are briefly mentioned. Second-harmonic generation in unidirectional composite plates subjected to thermal and impact damage was studied in Refs. 62 and 63, respectively. Li and Cho⁶⁴ also measured second-harmonic generation in a pipe. Choi et al.⁶⁵ used the axisymmetric $T(0,1)$ mode in an Alloy 617 pipe to generate third harmonics that are sensitive to the fatigue-creep damage that was present. Nucera and Lanza di Scalea⁶⁶ investigated nonlinear guided waves in solids subjected to constrained thermal expansion with a view of being able to characterize residual stresses due to the thermal expansion of rails.

5 Conclusions

Material and geometric nonlinearities distort passing guided waves, which cause self-interactions to generate higher harmonics at integer multiples of the excitation frequency and mutual interactions to generate combinational harmonics. Because propagating guided waves are confined to the dispersion curves, the selection of primary modes that generates internally resonant higher harmonics is a critical first

step that has been enabled by theoretical modeling. Internally resonant mode pairs are phase matched and have nonzero power flux, and unfortunately, are quite limited in number. Numerical simulations enable virtual experiments to be conducted without instrument nonlinearities and collection of data that is difficult to acquire from physical experiments. Simulations have shown that secondary modes once generated, propagate independent of the primary mode without the need for group velocity matching. Also, it was found that the interplay between the wavestructure of the primary mode and localized material degradation significantly affects the harmonic generation. Experiments have been conducted with a variety of transmitters and receivers that demonstrate the relevant features of higher harmonic guided waves: e.g., antisymmetric second-harmonic RL modes are not cumulative while symmetric second-harmonic RL modes are, and they are sensitive to various types of microstructural evolution. Thus, nonlinear guided waves have a strong potential for characterization of incipient damage. In order to achieve the potential of nonlinear guided waves, it seems expedient to correlate the higher harmonic generation with actual features of the material microstructure. Investigations to relate ultrasonic nonlinearity for bulk waves with material microstructure have been reported by numerous researchers.^{12–14,43,67,68} However, these 1-D analysis efforts may not be applicable for guided waves due to their three-dimensional nature. Recent investigations by the authors define an asymmetry parameter for mesoscale analysis that can be homogenized up to the continuum level.^{69,70} More research along these lines should enable a correlation between the higher harmonic generation and the evolution of the microstructure, which is incipient damage. This, in turn, will enable remaining life prediction at an early point in the service life of structural systems.

Acknowledgments

This material is based upon work supported by the National Science Foundation under Award number 1300562. Vamshi Chillara also acknowledges the support from the Penn State College of Engineering in the form of Distinguished Teaching Fellowship.

References

1. K.-Y. Jhang, "Nonlinear ultrasonic techniques for nondestructive assessment of micro damage in material: a review," *Int. J. Precis. Eng. Manuf.* **10**(1), 123–135 (2009).
2. Y. Zheng, R. G. Maev, and I. Y. Solodov, "Review/sythèse nonlinear acoustic applications for material characterization: a review," *Can. J. Phys.* **77**(12), 927–967 (2000).
3. M. Muller et al., "Nonlinear resonant ultrasound spectroscopy (NRUS) applied to damage assessment in bone," *J. Acoust. Soc. Am.* **118**(6), 3946–3952 (2005).
4. K.-A. Van Den Abeele, P. A. Johnson, and A. Sutin, "Nonlinear elastic wave spectroscopy (NEWS) techniques to discern material damage, part i: nonlinear wave modulation spectroscopy (NWMS)," *Res. Nondestr. Eval.* **12**(1), 17–30 (2000).
5. K.-A. Van Den Abeele et al., "Nonlinear elastic wave spectroscopy (news) techniques to discern material damage, part ii: single-mode nonlinear resonance acoustic spectroscopy," *J. Res. Nondestr. Eval.* **12**(1), 31–42 (2000).
6. K. E. Van Den Abeele et al., "Micro-damage diagnostics using nonlinear elastic wave spectroscopy (news)," *Ndt E Int.* **34**(4), 239–248 (2001).
7. J. H. Cantrell and W. T. Yost, "Nonlinear ultrasonic characterization of fatigue microstructures," *Int. J. Fatigue* **23**, 487–490 (2001).
8. P. P. Delsanto, *Universality of Nonclassical Nonlinearity*, Springer, New York (2006).
9. M. Breazeale and D. Thompson, "Finite-amplitude ultrasonic waves in aluminum," *Appl. Phys. Lett.* **3**(5), 77–78 (1963).

10. M. Breazeale and J. Ford, "Ultrasonic studies of the nonlinear behavior of solids," *J. Appl. Phys.* **36**(11), 3486–3490 (1965).
11. W. B. Gauster and M. Breazeale, "Ultrasonic measurement of the non-linearity parameters of copper single crystals," *Phys. Rev.* **168**(3), 655 (1968).
12. A. Hikata, B. B. Chick, and C. Elbaum, "Dislocation contribution to the second harmonic generation of ultrasonic waves," *J. Appl. Phys.* **36**(1), 229–236 (1965).
13. A. Hikata and C. Elbaum, "Generation of ultrasonic second and third harmonics due to dislocations. i," *Phys. Rev.* **144**(2), 469 (1966).
14. A. Hikata, F. Sewell, Jr., and C. Elbaum, "Generation of ultrasonic second and third harmonics due to dislocations. ii," *Phys. Rev.* **151**(2), 442 (1966).
15. K. Matlack et al., "Review of second harmonic generation measurement techniques for material state determination in metals," *J. Nondestr. Eval.*, 1–23 (2014).
16. M. Deng, "Cumulative second-harmonic generation accompanying nonlinear shear horizontal mode propagation in a solid plate," *J. Appl. Phys.* **84**(7), 3500–3505 (1998).
17. M. Deng, "Cumulative second-harmonic generation of lamb-mode propagation in a solid plate," *J. Appl. Phys.* **85**(6), 3051–3058 (1999).
18. B. A. Auld, *Acoustic Fields and Waves in Solids*, Robert E. Kreiger Publishing Company, Malabar, Florida (1990).
19. W. De Lima and M. Hamilton, "Finite-amplitude waves in isotropic elastic plates," *J. Sound Vib.* **265**(4), 819–839 (2003).
20. R. M. Bowen, *Introduction to Continuum Mechanics for Engineers*, Plenum Press, New York (1989).
21. M. Destrade and R. W. Ogden, "On the third- and fourth-order constants of incompressible isotropic elasticity," *J. Acoust. Soc. Am.* **128**(6), 3334–3343 (2010).
22. V. K. Chillara and C. J. Lissenden, "Interaction of guided wave modes in isotropic weakly nonlinear elastic plates: higher harmonic generation," *J. Appl. Phys.* **111**(12), 124909 (2012).
23. V. K. Chillara, "Higher harmonic guided waves in isotropic weakly non-linear elastic plates," Master's Thesis, The Pennsylvania State University (2012).
24. N. Matsuda and S. Biwa, "Phase and group velocity matching for cumulative harmonic generation in lamb waves," *J. Appl. Phys.* **109**(9), 094903 (2011).
25. M. F. Müller et al., "Characteristics of second harmonic generation of lamb waves in nonlinear elastic plates," *J. Acoust. Soc. Am.* **127**(4), 2141–2152 (2010).
26. Y. Liu, V. K. Chillara, and C. J. Lissenden, "On selection of primary modes for generation of strong internally resonant second harmonics in plate," *J. Sound Vib.* **332**(19), 4517–4528 (2013).
27. A. Srivastava and F. Lanza di Scalea, "On the existence of antisymmetric or symmetric lamb waves at nonlinear higher harmonics," *J. Sound Vib.* **323**(3), 932–943 (2009).
28. Y. Liu, C. J. Lissenden, and J. L. Rose, "Cumulative second harmonics in weakly nonlinear plates and shells," *Proc. SPIE* **8695**, 86950S (2013).
29. Y. Liu et al., "Third harmonic shear horizontal and Rayleigh lamb waves in weakly nonlinear plates," *J. Appl. Phys.* **114**(11), 114908 (2013).
30. W. J. de Lima and M. F. Hamilton, "Finite amplitude waves in isotropic elastic waveguides with arbitrary constant cross-sectional area," *Wave Motion* **41**(1), 1–11 (2005).
31. A. Srivastava and F. Lanza di Scalea, "On the existence of longitudinal or flexural waves in rods at nonlinear higher harmonics," *J. Sound Vib.* **329**(9), 1499–1506 (2010).
32. A. Srivastava et al., "Higher harmonic generation in nonlinear waveguides of arbitrary cross-section," *J. Acoust. Soc. Am.* **127**(5), 2790–2796 (2010).
33. V. K. Chillara and C. J. Lissenden, "Analysis of second harmonic guided waves in pipes using a large-radius asymptotic approximation for axis-symmetric longitudinal modes," *Ultrasonics* **53**(4), 862–869 (2013).
34. Y. Liu et al., "Interaction of torsional and longitudinal guided waves in weakly nonlinear circular cylinders," *J. Acoust. Soc. Am.* **133**(5), 2541–2553 (2013).
35. Y. Liu, C. J. Lissenden, and J. L. Rose, "Higher order interaction of elastic waves in weakly nonlinear hollow circular cylinders. i. analytical foundation," *J. Appl. Phys.* **115**(21), 214901 (2014).
36. Y. Liu et al., "Higher order interaction of elastic waves in weakly nonlinear hollow circular cylinders. ii. physical interpretation and numerical results," *J. Appl. Phys.* **115**(21), 214902 (2014).
37. C. Nucera and F. Lanza di Scalea, "Nonlinear semianalytical finite-element algorithm for the analysis of internal resonance conditions in complex waveguides," *J. Eng. Mech.* **140**(3), 502–522 (2013).
38. N. Matsuda and S. Biwa, "Frequency dependence of second-harmonic generation in lamb waves," *J. Nondestr. Eval.* **33**(2), 169–177 (2014).
39. R. Radecki et al., "Investigation on high-order harmonic generation of guided waves using local computation approaches: Theory and comparison with analytical modelling," in *EWSHM-7th European Workshop on Structural Health Monitoring* (2014).
40. V. K. Chillara and C. J. Lissenden, "Nonlinear guided waves in plates: a numerical perspective," *Ultrasonics* **54**(6), 1553–1558 (2014).
41. V. K. Chillara and C. J. Lissenden, "Nonlinear guided waves in plates undergoing localized microstructural changes," in *41st Annual Review of Progress in Quantitative Nondestructive Evaluation*, Vol. 1650, pp. 1561–1569, AIP Publishing (2015).
42. N. Rauter and R. Lammering, "Numerical simulation of elastic wave propagation in isotropic media considering material and geometrical nonlinearities," *Smart Mater. Struct.* **24**(4), 045027 (2015).
43. J. H. Cantrell, "Substructural organization, dislocation plasticity and harmonic generation in cyclically stressed wavy slip metals," *Proc. R. Soc. London Ser. A* **460**(2043), 757–780 (2004).
44. M. Deng, P. Wang, and X. Lv, "Experimental verification of cumulative growth effect of second harmonics of lamb wave propagation in an elastic plate," *Appl. Phys. Lett.* **86**(12), 124104 (2005).
45. M. Deng, P. Wang, and X. Lv, "Experimental observation of cumulative second-harmonic generation of lamb-wave propagation in an elastic plate," *J. Phys. D Appl. Phys.* **38**(2), 344 (2005).
46. C. Bernes et al., "Experimental characterization of material nonlinearity using lamb waves," *Appl. Phys. Lett.* **90**(2), 021901 (2007).
47. C. Bernes et al., "Nonlinear lamb waves for the detection of material nonlinearity," *Mech. Syst. Sig. Process.* **22**(3), 638–646 (2008).
48. K. H. Matlack et al., "Experimental characterization of efficient second harmonic generation of lamb wave modes in a nonlinear elastic isotropic plate," *J. Appl. Phys.* **109**(1), 014905 (2011).
49. C. Pruell et al., "Evaluation of plasticity driven material damage using lamb waves," *Appl. Phys. Lett.* **91**(23), 231911 (2007).
50. C. Pruell et al., "A nonlinear-guided wave technique for evaluating plasticity-driven material damage in a metal plate," *NDT E Int.* **42**(3), 199–203 (2009).
51. C. Pruell et al., "Evaluation of fatigue damage using nonlinear guided waves," *Smart Mater. Struct.* **18**(3), 035003 (2009).
52. T.-H. Lee, I.-H. Choi, and K.-Y. Jhang, "The nonlinearity of guided wave in an elastic plate," *Mod. Phys. Lett. B* **22**(11), 1135–1140 (2008).
53. Y. Liu et al., "Experimental investigation of symmetry properties of second harmonic lamb waves," *J. Appl. Phys.* **111**(5), 053511 (2012).
54. C. Lissenden et al., "Effect of localized microstructure evolution on higher harmonic generation of guided waves," *J. Nondestr. Eval.* **33**(2), 178–186 (2014).
55. C. Lissenden, Y. Liu, and J. Rose, "Use of non-linear ultrasonic guided waves for early damage detection," *Insight Non-Destr. Test. Cond. Monit.* **57**(4), 206–211 (2015).
56. M. Hong et al., "Modeling nonlinearities of ultrasonic waves for fatigue damage characterization: theory, simulation, and experimental validation," *Ultrasonics* **54**(3), 770–778 (2014).
57. M. Hong et al., "Locating fatigue damage using temporal signal features of nonlinear lamb waves," *Mech. Syst. Sig. Process.* **60**, 182–197 (2015).
58. F. Aymerich and W. Staszewski, "Impact damage detection in composite laminates using nonlinear acoustics," *Compos. Part A* **41**(9), 1084–1092 (2010).
59. F. Semperlotti, K. Wang, and E. Smith, "Localization of a breathing crack using nonlinear subharmonic response signals," *Appl. Phys. Lett.* **95**(25), 254101 (2009).
60. G.-W. Kim et al., "Localization of breathing cracks using combination tone nonlinear response," *Smart Mater. Struct.* **20**(5), 055014 (2011).
61. Y. Shen and V. Giurgiutiu, "Predictive simulation of nonlinear ultrasonics," *Proc. SPIE* **8348**, 83482E (2012).
62. W. Li, Y. Cho, and J. D. Achenbach, "Detection of thermal fatigue in composites by second harmonic lamb waves," *Smart Mater. Struct.* **21**(8), 085019 (2012).
63. N. Rauter and R. Lammering, "Impact damage detection in composite structures considering nonlinear lamb wave propagation," *Mech. Adv. Mater. Struct.* **22**(1–2), 44–51 (2015).
64. W. Li and Y. Cho, "Thermal fatigue damage assessment in an isotropic pipe using nonlinear ultrasonic guided waves," *Exp. Mech.* **54**(8), 1309–1318 (2014).
65. G. Choi, Y. Liu, and C. J. Lissenden, "Nonlinear guided waves for monitoring microstructural changes in metal structures," in *Proc. ASME 2015 Pressure Vessels and Piping Conf.*, ASME International, PVP45292 (2015).
66. C. Nucera and F. Lanza di Scalea, "Nonlinear wave propagation in constrained solids subjected to thermal loads," *J. Sound Vib.* **333**(2), 541–554 (2014).
67. J. H. Cantrell and W. T. Yost, "Acoustic harmonic generation from fatigue-induced dislocation dipoles," *Philos. Mag. A* **69**(2), 315–326 (1994).
68. Y. Xiang et al., "Effect of precipitate-dislocation interactions on generation of nonlinear lamb waves in creep-damaged metallic alloys," *J. Appl. Phys.* **111**(10), 104905 (2012).
69. V. K. Chillara and C. J. Lissenden, "Towards a micro-mechanics based understanding of ultrasonic higher harmonic generation," *Proc. SPIE* **9438**, 94380R (2015).

70. V. K. Chillara and C. J. Lissenden, "On some aspects of material behavior relating microstructure and ultrasonic higher harmonic generation," *Int. J. Eng. Sci.* **94**, 59–70 (2015).

Vamshi Krishna Chillara is a PhD student (graduation, August 2015) in the Department of Engineering Science and Mechanics at Penn State. He received his MS degree in engineering mechanics from Penn State in 2012. His research interests include ultrasonic sensing for nondestructive evaluation and structural health monitoring (SHM) of materials, nonlinear acoustics, wave propagation in multiscale materials, and phononics. Currently, he is a student member of SPIE and IEEE.

Cliff J. Lissenden is a professor of engineering science and mechanics at Penn State. He joined the Department of Engineering Science and Mechanics in 1995 and added an appointment in acoustics in 2011. He is an ASME fellow and was a founder of the Ben Franklin Center of Excellence in SHM, which is the primary area of his research. Within SHM, his areas of specialization are guided wave ultrasonics and mechanical behavior of materials.